Article:
Graves, A. orcid.org/0000-0003-4835-3772, Salmasi, A., Graham, S.J. orcid.org/0000-0002-1296-1680 et al. (5 more authors) (2023) An experimental and theoretical investigation on Ti-5553/WC–Co(6%) chemical interactions during machining and in diffusion couples. Wear, 516-517. 204604. ISSN: 0043-1648

https://doi.org/10.1016/j.wear.2022.204604

Wear 516-517 (2023) 204604

Contents lists available at ScienceDirect

Wear

journal homepage: www.elsevier.com/locate/wear

An experimental and theoretical investigation on Ti-5553/WC–Co(6%) chemical interactions during machining and in diffusion couples

Alex Graves [a,*], Armin Salmasi [b,*], Simon J. Graham [a], Wei Wan [c], Changhong Xiao [c], Martin Jackson [a], Henrik Larsson [b], Susanne Norgren [c,d]

[a] Department of Materials Science and Engineering, The University of Sheffield, Sir Robert Hadfield Building, Mappin Street, Sheffield, S1 3JD, United Kingdom
[b] Department of Materials Science and Engineering, KTH Royal Institute of Technology, SE-100 44 Stockholm, Sweden
[c] AB Sandvik Coromant R&D, SE-126 80 Stockholm, Sweden
[d] Department of Mechanical Engineering Sciences, Division of Production and Materials Engineering, Lund University, SE-223 62 Lund, Sweden

ARTICLE INFO

Keywords:
Titanium
Turning
WC–Co
Tool wear
TEM
Thermodynamic simulation

ABSTRACT

Chemical interactions that drive crater wear in turning are often studied using diffusion couples where the tool and workpiece are fixed. In contrast, in actual turning, there is a constant supply of new workpiece material at the tool-chip interface. In this work, diffusion simulations of a WC–Co(6%) and Ti–5Al–5V system were conducted, with constant replenishment of titanium at the interface (open system) and a fixed amount of material (closed system). The simulations showed that the formation of W(bcc), η-phase, and TiC is dependent on the activity of C and the permeability of Co and C in titanium. Scanning and transmission electron microscopy-based techniques were used to analyse a Ti–5Al–5V–5Mo–3Cr and WC–Co(6%) diffusion couple and a worn WC–Co(6%) insert. The sequence of phases in the closed system simulation was similar to that observed in the diffusion couple. The open system simulation indicated that W(bcc) can form at WC–WC boundaries (where Co is low) within the subsurface of a WC–Co(6%) that has adhered titanium, and at the WC/Ti interface. Additionally, high densities of stacking faults and dislocations were found within subsurface WC grains, indicating a significant reduction of the tool's integrity.

1. Introduction

The aerospace industry is under pressure to implement low density, high strength materials like titanium alloys in aircraft to reduce weight and reduce fuel usage. The properties of titanium alloys are dependent on the α (hcp) and β (bcc) phase volume and distribution which is controlled via alloying additions and through processing. Ti–6Al–4V (Ti-64) is an $\alpha + \beta$ alloy utilised heavily for engine and aero-structural components. Ti–5Al–5V–5Mo–3Cr (Ti-5553) is a metastable β alloy which has superior strength and fatigue properties when compared to Ti-64, making it ideal for critical components such as landing gears [1]. In general, high strength, low thermal conductivity and high chemical reactivity make titanium alloys difficult to machine as evidenced by high forces, rapid tool wear and poor chip morphology [2]. For the case of the metastable β titanium alloys which exhibit higher strength and chemical reactivity with cutting tool materials, machinability can be considerably worse than in $\alpha + \beta$ alloys [3].

WC–Co is the primary cutting tool material used for machining titanium alloys due to the requirement of high toughness, fatigue resistance and high compressive stress. Such tool material also performs well at elevated temperatures, required during titanium machining, which can reach temperatures of 900–1050 °C [4–6]. The anisotropic structure of WC means that the substrate within WC–Co tools consists of irregular WC grains within a Co matrix. The WC–Co based system has been reported to stay in stable equilibrium at temperatures exceeding 1000 °C [7]. Between each of the WC grains remains a Co mono-layer that forms during sintering [8]. During such sintering, residual stresses are accommodated through plastic deformation and thus the defect density within the WC is low [9]. In more recent developments Östberg et al. [10], for the area of steel turning, has been able to detect the Co mono-layer between the WC–WC grains using transmission electron microscope (TEM) and has used Ab initio calculations to find that during plastic deformation, defects propagate along low energy planes within the WC grains at WC–WC grain boundaries.

Although WC–Co tools exhibit superiority for machining titanium, the wear rate is still relatively high [2,11]. Crater wear, which is driven by the chemical and diffusion interaction between the tool substrate and workpiece material on the rake face, is the primary wear type responsible for the failure of WC–Co tools in the machining of titanium

* Corresponding authors.
E-mail addresses: alexander.graves@sandvik.com (A. Graves), salmasi@kth.se (A. Salmasi).

https://doi.org/10.1016/j.wear.2022.204604
Received 17 March 2022; Received in revised form 16 December 2022; Accepted 19 December 2022
Available online 28 December 2022

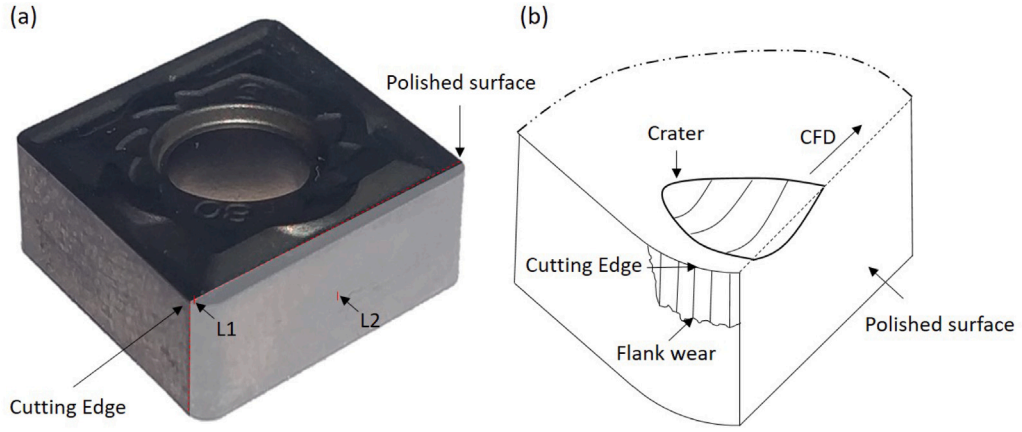

Fig. 1. (a) Modified image of an unused H13A insert. The region removed during polishing is highlighted. L1 and L2 mark the locations where lamellae were removed via FIB for TEM analysis. (b) A schematic diagram of the polished region sectioned within the crater near the cutting edge.

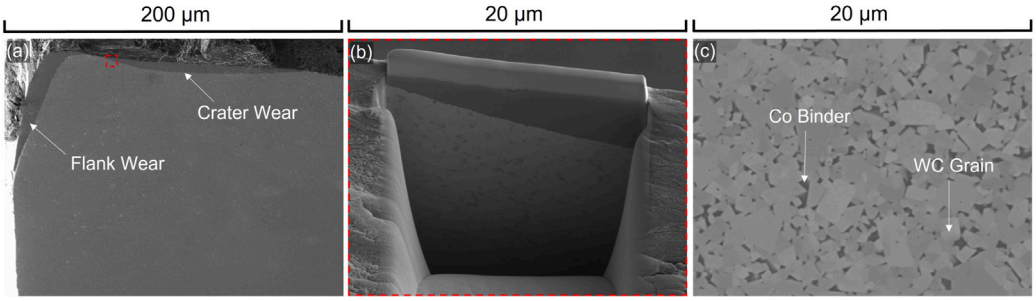

Fig. 2. Secondary electron images: (a) The polished insert and location of FIB preparation. (b) The remaining surface before TEM lamella removal. (c) The tool substrate.

alloys. As the tool wears the crater grows at a relatively consistent rate, however, upon reaching a critical size, the cutting edge becomes prone to plastic deformation, and the flank wear rate increases rapidly which leads to rapid tool failure [4]. The mechanism by which the crater develops on the rake face of the cutting tool has been investigated in several studies [12–18]. Both Hatt et al. [15] and Ramirez et al. [16] investigated the chemical interactions that drive crater wear by manufacturing diffusion couples containing WC–Co and titanium alloys. Hatt et al. established the relationship between alloy β stability and the rate of tool wear. Ramirez et al. highlighted the importance and behaviour of Co at the interface between the substrate and workpiece. However, the results obtained by using diffusion couples differ significantly to those obtained from the analysis of craters formed by machining titanium. In diffusion couples, a substantial TiC layer forms at the interface below which brittle η-phases M6C and M12C have been evidenced [14], whereas, in craters formed during machining, neither a continuous TiC layer nor η-phase has been detected. If a consistent TiC layer were to form it would retard the reaction between the tool and work-piece thus slowing the crater growth and prolonging tool life. The presence of η-phase would indicate a reduction in substrate integrity and could lead to more rapid wear and/or premature breakages.

The difference between the dynamic machining crater formation and the diffusion couple system is highlighted by Kaplan et al. [13] who investigate both cases. During machining, the chip slides over the rake face of the tool causing tool material to be removed via abrasion and stick–slip adhesion. In either the absence of an adhesive layer or when a fully equilibrated adhesive layer is formed, the activity of elements at the tool/workpiece interface is close or equal to the activity of elements in Ti-5553 alloy. Therefore, once substantial material adheres to the crater, diffusion-driven dissolution and decarburisation of the WC–Co accelerates and becomes continuous [13,17,19]. Highly abrasive carbide particles form within the crater at the tool-adhered material interface due to the interaction of carbon with the titanium and its alloying additions and facilitate breakage of decarburised W(bcc) from the interface. Although decarburisation of the tool material is restricted at WC–titanium interfaces where there is no Co and where W(bcc) forms; mediating the C activity, continuous decarburisation of the tool has been shown to occur at the WC–titanium interface at WC grain boundaries which are Co rich [17]. Recent work by Lindvall et al. has evidenced the formation of reaction products such as Co_3W and $TiCo_2$ on the rake and flank face of the tool after turning Ti-64 both of which can be expected to retard the direct dissolution of WC at the interface [18].

It is important that the reason behind the differences between those results obtained in diffusion couples and those obtained by analysing craters are resolved to provide efficacy to results obtained using diffusion couples. Resolving the differences also provides a good method of further understanding the mechanism by which tool material is lost during crater wear. In this study, STEM (scanning transmission electron microscope) and TEM energy-dispersive X-ray spectroscopy (TEM-XEDS) is used to analyse and characterise the tool substrate below the tool-workpiece interface in the crater region. In addition, a diffusion couple was created using an identical, but unused copy of the worn insert. Scanning electron microscope (SEM) and EPMA (electron probe microanalyzer) wavelength dispersive spectroscopy (WDS) i.e. EPMA-WDS were used to characterise and analyse the interface of the diffusion couple. For the first time in the literature, the differences between the interface that forms in the crater [13,17,19], and the interface that forms within diffusion couples have been resolved using simulation.

2. Experimental details

2.1. Turning of Ti-5553

In this study, a single billet of a metastable beta alloy, Ti–5Al–5V–5Mo–3Cr (Nominal Composition wt. %) was used. The billet was sub

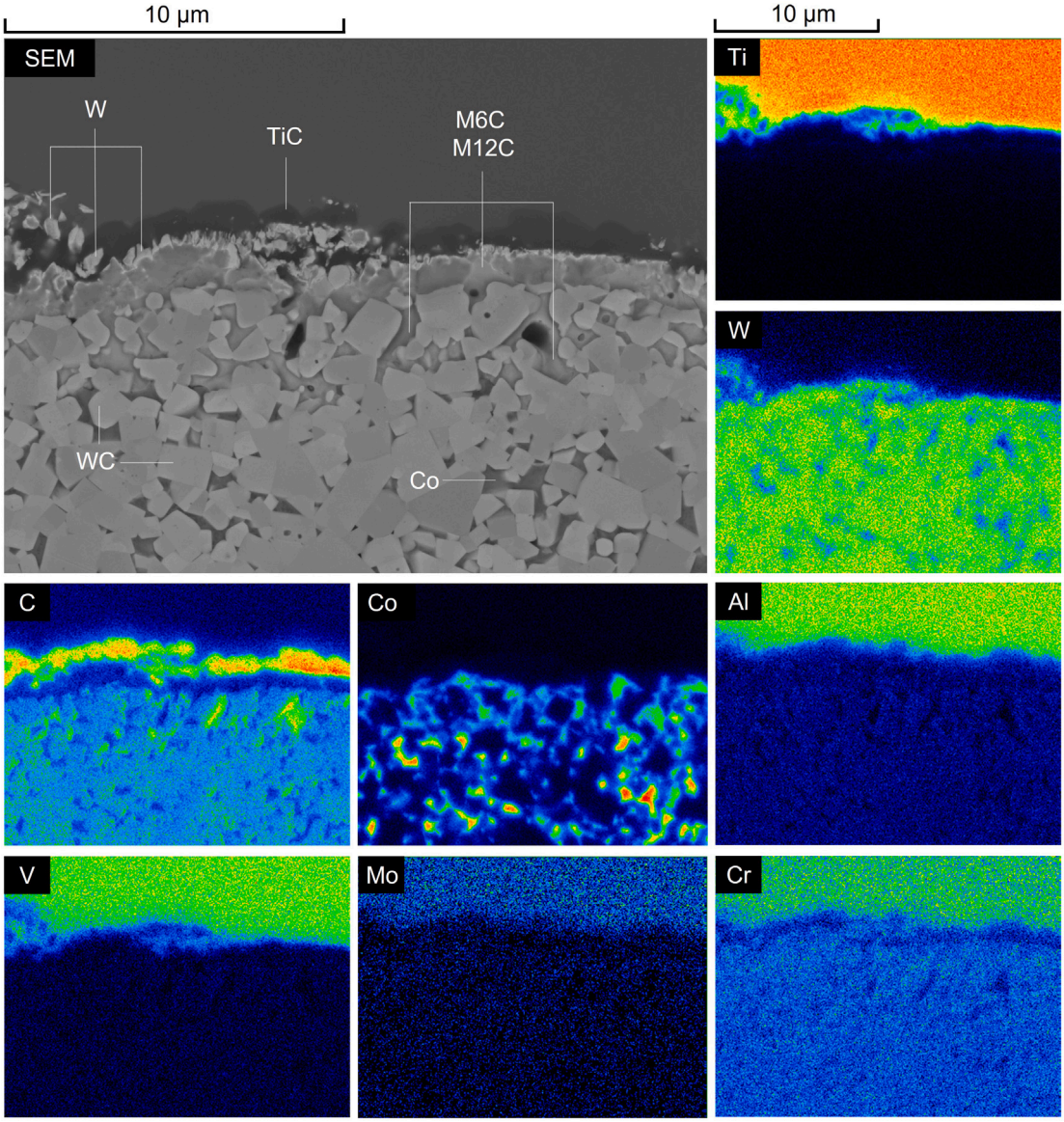

Fig. 3. A labelled SEM image of the interface formed in the diffusion couple between the WC–Co substrate and Ti-5553. Also included are WDS maps obtained using the EPMA for Ti, W, C, Co, Al, V, Mo and Cr.

transus heat treated and aged, had a hardness of 410 Hv and a diameter of 150 mm. The outer diameter of the billet material was turned on a Cincinnati Hawk SL 300 Lathe where the billet was clamped using a three-jaw chuck and supported using a centre support to maintain stability. The cutting inserts used for the turning operation were WC–Co uncoated inserts; H13A CNMG 12 04 08-SM. These inserts have a 0-degree clearance angle and a negative 25-degree rake angle. The WC grain size measured 1-1.3 µm, the cobalt content was 6 wt%. The Vickers hardness of the inserts was 1600 Hv. The edge rounding of the insert used for testing was 32.5 µm. The cutting insert was held in a C5-DCLNL-35060-12 tool holder which resulted in the cutting edge angle being 95 degrees and the tool lead angle being −5 degrees. The turning operation was conducted for 900 s with a single insert at a cutting speed (v_c), of 70 m/min, a radial depth-of-cut (a_p), of 1 mm and a feed rate (f_n), of 0.1 mm/rev. Throughout the test 5% concentration Hocut 795B-EU water emulsion, flood coolant was supplied through the tool holder onto the cutting edge at 5.4 L/min at a pressure of 8 bar.

2.2. Sample preparation and observation

To investigate the crater region on the rake face of the cutting insert the tool was mounted in bakelite and the face perpendicular to the flank was polished on a neoprene surface using a diamond suspension solution with an applied force of 20 N. Fig. 1(a) shows a modified photograph of the unused H13A insert, the region which has been removed during polishing is highlighted. In Fig. 1(b) a schematic diagram of the cutting tool corner is presented and shows how the polished surface intersects the crater which forms behind the tool's cutting edge. Once sectioned the crater could be easily located and samples could be prepared for TEM. Lamella samples were sectioned from the L1 and L2 locations as marked in Fig. 1(a) on a Thermo-Fisher-Scientific Helios 650 dual-beam focused ion beam (FIB) using the lift out technique. Prior to using FIB, a protective platinum layer was applied to the locations in order to preserve the surface. Once extracted the lamellae were then attached to a copper grid and thinned to electron transparency with the ion beam. Fig. 2(a) shows a secondary electron image of the polished surface and the sectioned crater. Fig. 2(b) shows the

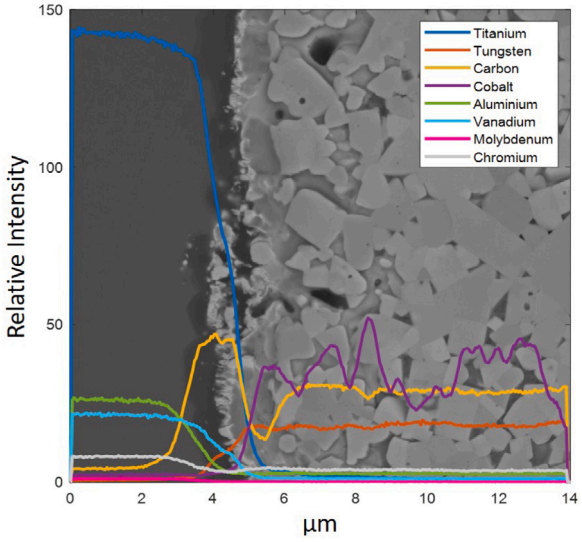

Fig. 4. Results from the WDS EPMA area scan overlaid over an SEM image of the scanned area. The elements which are included are Ti, W, C, Co, Al, V, Mo and Cr.

remaining crater and tool interface. Fig. 2(c) shows an SEM image from an undamaged region of the tool substrate in which both WC grains and Co binder can be clearly differentiated. TEM observations of the lamellae were made on a double-corrected ThermoFisherScientific Titan G2 transmission electron microscope operated at 300 kV. Bright-field (BF) and dark-field (DF) scanning transmission electron microscope (STEM) images were collected on Gatan STEM detectors. STEM X-EDS data were collected on the Bruker SuperX detector.

In the first instance, TEM is used to obtain dark field (DF) and bright field (BF) STEM images by scanning an electron probe over the lamella extracted from both the subsurface and centre of the tools, measuring the intensity of the diffracted electrons after transmission. Then TEM is utilised to obtain electron diffraction patterns (EDP) from WC grains and WC grain boundaries enabling the phase at such locations to be identified. Further to this at grain boundaries, X-EDS is used to observe the distribution of Co and W at grain boundaries. Fourier filtering and masking are used to identify the nature of defects within the WC grains near the crater subsurface.

2.3. Ti-5553 and WC-Co diffusion couple

As part of the investigation a diffusion couple was created using Ti-5553 and a H13A CNMG 1204 08-SM insert. Prior to manufacturing the diffusion couple, the flank of the insert was polished away using the same method described in 2.2, so the insert resembled the insert used in the turning experiment, shown in Fig. 1. The diffusion couple was then created using FAST in the FCT Systeme HP D 25 SPS furnace at the University of Sheffield. To make the sample, the insert was placed into a graphite mould with a 20 mm internal diameter. Then, 20 g of Ti-5553 powder (particle size 45-150 μm) was poured into the mould to completely surround the insert. During the process, a constant pressure and temperature, 35 MPa and 1000 °C (100 °C/min ramp rate), were applied causing the powder to consolidate around the insert. Then the sample was held at 35 MPa and 1000 °C for a dwell time of 120 min to study the diffusion behaviour at the interface between the insert and the Ti-5553. The cooling rate of the sample was relatively quick at 100 °C/min plus from 1000 °C to 400 °C. After cooling the diffusion couple was sectioned in half, using a Struers Secotom-50 equipped with a diamond-tipped cutting blade creating a cross-section of the polished surface along the L1 line shown within Fig. 1(a). Once sectioned the diffusion couples were mounted in conductive Bakelite using a Simplimet 2000 and ground and polished to a mirror finish using a Tegramin 30 machine. During this process a series silicon carbide grit papers (P400 to P2500), were used, followed by a 6 μm, then 3 μm diamond suspension on a neoprene surface. Once the diffusion couple was prepared SEM was carried out on a Hitachi SU7000 using a backscatter electron detector that renders Z-contrast. Then, WDS was carried out using a JEOL JXA-8530F electron probe micro analyser (EPMA).

3. Modelling details

3.1. Diffusion model

The DICTRA homogenisation model [20,21], was used for 1D simulations of the diffusion-reaction process taking place during the heat treatment of the diffusion couple and during the turning experiment. DICTRA is coupled to the Thermo-Calc software [22], which provides all necessary thermodynamic and kinetic data during simulations.

Diffusion was assumed to take place only in the fcc and bcc solid solution phases, though all stable phases affect the process as outlined below. From a computational point of view, through a coarse-graining homogenisation procedure, the multiphase problem is transformed into a single-phase problem. In the homogenisation model, the basic expression for the flux of element k in a given phase α is

$$J_k^\alpha = -M_k^\alpha c_k^\alpha \nabla \mu_k^\alpha, \tag{1}$$

where M_k^α, c_k^α and μ_k^α denote mobility, concentration and chemical potential of element k in the α phase, respectively. The permeability of the α phase with respect to element k is given by

$$\Gamma_k^\alpha = M_k^\alpha c_k^\alpha. \tag{2}$$

In the coarse-graining procedure, the assumption is that the system is locally fully equilibrated at all times, thus the chemical potentials of each constituent is the same in all locally stable phases. The local phase fractions, phase compositions, etc. are also obtained from the assumption of local equilibration given the overall local composition, temperature, and pressure. One denotes the effective permeability of the multiphase mixture $\Gamma_k^\star$, the effective permeability can, for example, be obtained from a rule-of-mixture where f^ϕ is the local volume fraction of the ϕ phase is then written as

$$\Gamma_k^\star = \sum_\phi f^\phi \Gamma_k^\phi \tag{3}$$

the flux through the multiphase mixture is then written as

$$J_k = -\Gamma_k^\star \nabla \mu_k^{l.eq.} \tag{4}$$

where the $l.eq.$ indicates the assumption of a locally equilibrated structure. Details of the implementation of the homogenisation model is discussed elsewhere [20,21].

3.2. Model setup

Mo and Cr are not considered in the modelling to simplify the calculations and have a general view of the interaction between Ti–Al(5%)-V(5%) and cemented carbide. Therefore, simulations only consider diffusion reaction between a WC–Co(6%) cutting tool and a Ti–Al(5%)-V(5%) alloy. Simulations were performed for 3600 s at 1000 °C using the TCFE9 thermodynamic database [23], and the MOBFE5 mobility database [24]. The diffusion taking place during heating and cooling was minimal and therefore not included in the simulations.

Two different types of simulations were performed. To simulate a system similar to that of the diffusion couple, the composition in the left part of the domain was set to WC–Co(6%), and in the right-hand part, to Ti–Al(5%)-V(5%) with a sharp step in between. To simulate a system that resembles turning the composition throughout the domain was set to WC–Co(6%), and the interaction with Ti–Al(5%)-V(5%)

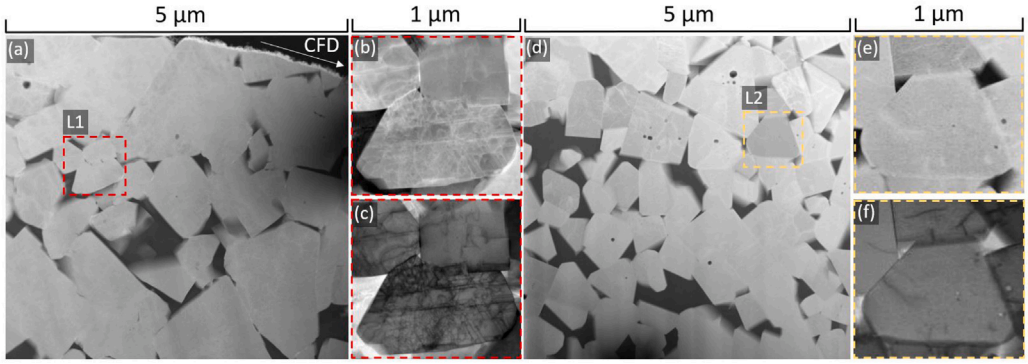

Fig. 5. DF-STEM (a,b, d, e) and BF-STEM (c,f) images. (a, b, c) are from 4 µm below crater surface and (d, e, f) are from the centre of insert. The arrow marked with CFD in (a) indicates the chip flow direction.

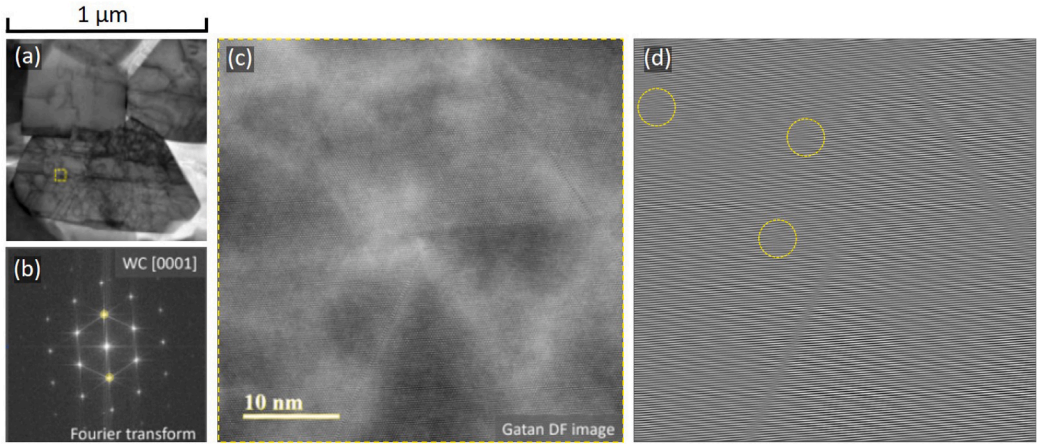

Fig. 6. (a) BF-STEM image of WC grain 4 µm below the crater interface. (b) Fourier transform of (c), which is a DF-STEM image of location marked in (a). (d) Fourier-filtered image of (c) using the 11–20 reflections as marked in (b), showing the location of stacking faults within the lattice at the location marked in (a).

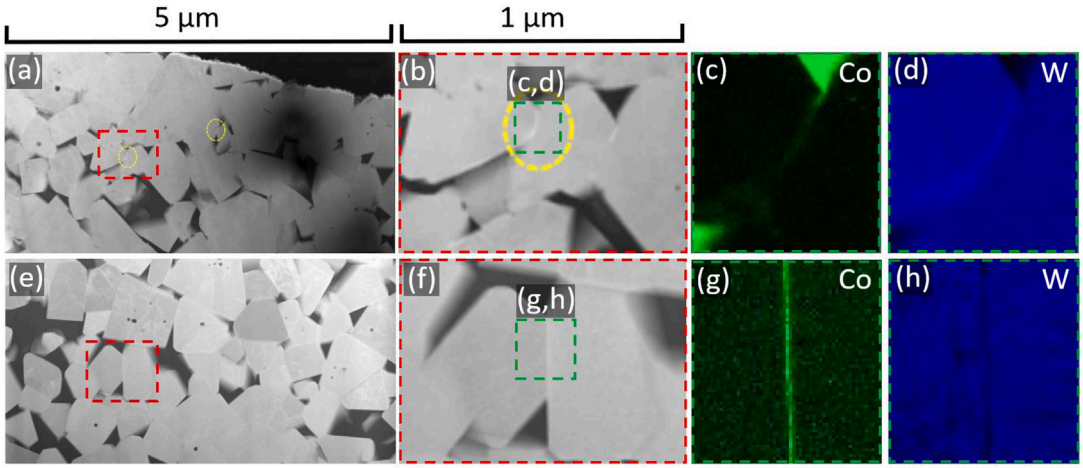

Fig. 7. (a, b) DF-STEM images of the WC substrate crater subsurface. (c,d) are STEM X-EDS maps for Co an W from the location marked in green on (b). (e, f) DF-STEM images of the WC substrate at the centre of the tool. (g,f) are STEM X-EDS maps for Co an W from the location marked in green on (f). (For interpretation of the references to colour in this figure legend, the reader is referred to the web version of this article.)

workpiece was modelled with activity boundary conditions. The compositions which were used in modelling diffusion couples are listed in Table 1.

For both types of simulations, relevant boundary conditions were applied individually for each element. In the diffusion couple simulation at the left-hand side of the WC–Co(6%) the activities of W, C, and Co are fixed and at the right-hand side of the Ti–Al(5%)-V(5%) the activities of Al, C, Co, Ti, V are fixed. The boundary diffusivities were selected in accordance with the tungsten carbide/titanium alloy compositions, respectively. For the roughly fixed C activity simulation, these boundary conditions were also applied. The main difference being that the initial composition corresponds to WC–Co(6%) over the whole domain. In addition, precipitation of new phases during the simulation is detected automatically.

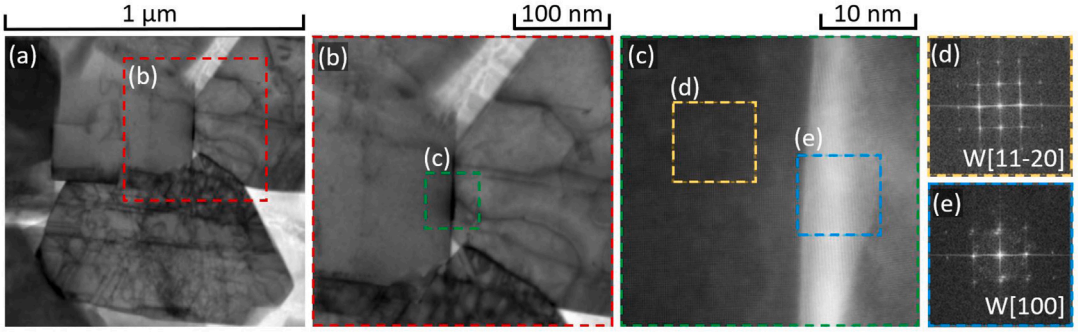

Fig. 8. (a) BF-STEM image of WC grain 4 μm below the crater interface. (b) BF-STEM image of WC–WC grain boundary from (a). (c) High magnification BF-STEM image of WC–WC grain boundary. (d) and (e) are diffraction patterns from the yellow and blue locations given in (c) and show WC [11-20] and W [001] respectively. (For interpretation of the references to colour in this figure legend, the reader is referred to the web version of this article.)

Table 1
Simulated compositions of Ti–Al(5%)-V(5%) and WC–Co(6%).

Mole fraction	Al	C	Co	Ti	V	W
WC–Co(6%)	1.0E−04	4.5E−01	9.6E−02	1.0E−04	1.0E−04	Balance
Ti–Al(5%)-V(5%)	8.6E−02	1.0E−04	1.0E−04	8.7E−01	4.5E−02	Balance

4. Results

4.1. Experimental observations — diffusion couple

The interface between the WC–Co substrate and Ti-5553 is evident in the SEM image and WDS maps for Ti, W, C, Co, Al, V, Mo and Cr shown in Fig. 3. At the bottom of the SEM image, both the WC grains and the Co binder can be seen. These regions can be further identified by observing the W, C and Co WDS maps. The Ti-5553, at the top of the SEM image, is identifiable from the Ti, Al, V, Mo and Cr maps. In the SEM image, on the Ti-5553 side of the interface, there is a dark layer, rich in Ti and C. There is a high likelihood that this layer is TiC. Small white flecks of W(bcc) [17], rich in W and not C, are also evident in the SEM image in and around the TiC. Before the W(bcc) detaches from the substrate it is present as a white layer below the TiC, typically described to have a fringe-like morphology. Below this, there is a probable layer of M6C and M12C η-phase. Each of these phases exhibit a slightly lighter and darker contrast respectively. The η-phase is present up to 10 μm below the interface where the Co binder phase existed previously. This is supported by the fact that in the Co map there are more intense zones of Co below the η-phase. Fig. 4 shows the intensity of Ti, W, C, Co, Al, V, Mo and Cr across the interface as a line. The lines are constructed from data measured from the whole area, on which they are overlaid. The C trace in this figure further supports the η-phase hypothesis since after a peak in C due to the TiC layer there is a significant dip in C before it levels out in the substrate.

4.2. Experimental observations — turning

Turning Ti-5553 for 900 s has resulted in the formation of a crater, which can be seen in Fig. 2(a), on the rake face of the tool. The results presented in this section will be used to determine to what extent tool integrity is impacted within the subsurface in the crater. To do so a typical WC grain from 4 μm below the crater surface at L1, is compared to a similar grain at the centre of the tool, at L2. The position of L1 and L2 are indicated in Fig. 1(a). The quantity and type of defects are compared and the loss of carbon from below the subsurface of the tool is investigated via STEM X-EDS and EDP analysis.

Fig. 5 contains a BF-STEM and DF-STEM image of a WC grain 4 μm below the crater. Fig. 5(a) is a DF-STEM taken from L1, which is from the crater as shown in Fig. 2(a). Fig. 5(b) and (c) are higher magnification DF and BF STEM images of the location marked in Fig. 5(a). Fig. 5(d) is the DF-STEM taken from L2. Fig. 5(e) and (f) are the corresponding DF and BF stem images of the grain highlighted in Fig. 5(d). There is a significant difference in the number of defects present in the WC grain that is in the subsurface of the crater.

In Fig. 6(a) a location is selected for higher resolution analysis of the defects within the grain presented in Fig. 6(c). Fig. 6(b) shows the Fourier transform of Fig. 6(c) which identifies the phase as WC [0001]. The DF image presented in Fig. 6(c) is a high resolution of the zone marked in Fig. 6(a). To filter the image to show the 010 lattice a mask was applied on the two points highlighted in yellow in Fig. 6(b) and the result of this is shown in Fig. 6(d). Three locations where stacking faults have been identified are marked. In addition, 5 dislocations can be seen within the image. Considering there to be 10 defects per 43 x 43 nm (size of image) yields a rough 'defect density' of $5 \cdot 10^{15}/\mathrm{m}^2$. Although the exact density was not calculated for other locations, observation of other areas close to this depth within the subsurface showed that there were many WC grains with comparable amounts of similar defects within the vicinity.

Two locations were investigated within the subsurface of the crater Fig. 7 (a, b, c, d) and centre of the tool Fig. 7 (e, f, g, h) in order to compare STEM X-EDS at WC grain boundaries for the different locations. Within Fig. 7(b) and (f) a region of higher contrast can be seen at the grain boundaries. This high contrast resembles the crater interface (seen in Fig. 7(a)), between the tool and the workpiece where W(bcc) has formed. For the case of both grain boundaries, a thin film of Co is present in Fig. 7(c) and (g). The W maps are not so similar, there is a slight increase in W observed at the boundary in Fig. 7(d), i.e within the subsurface of the crater whereas for the centre of the tool there is a lack of W at the grain boundary shown in Fig. 7(h) by the dark line. This suggests the formation of W(bcc) at WC grain boundaries within the crater subsurface but not deeper into the bulk of the tool. The results proved repeatable since examining two additional locations for both the subsurface and the centre of the tool yielded similar results.

To investigate whether there was W(bcc) forming at grain boundaries high-resolution STEM images and Fourier transforms were obtained from the location identified in Fig. 8 (a,b,c). The Fourier transforms in Fig. 8(d) and (e) are from the grain and grain boundary respectively. As should be the case Fig. 8(d) can be indexed as WC [11–20], Fig. 8(e), on the other hand, can be indexed as W [001] and proves the formation of W(bcc) at 4 μm below the crater subsurface between WC grain boundaries.

4.3. Simulation results

At 1000 °C there is high solubility and anomalously fast diffusion of Co in Ti–Al(5%)-V(5%) (see Fig. 9). Therefore, Co diffusion does not trigger any phase transformation on the Ti–Al(5%)-V(5%) side, i.e., bcc remains stable. Hence, phase transformations can only be observed in the tungsten carbide.

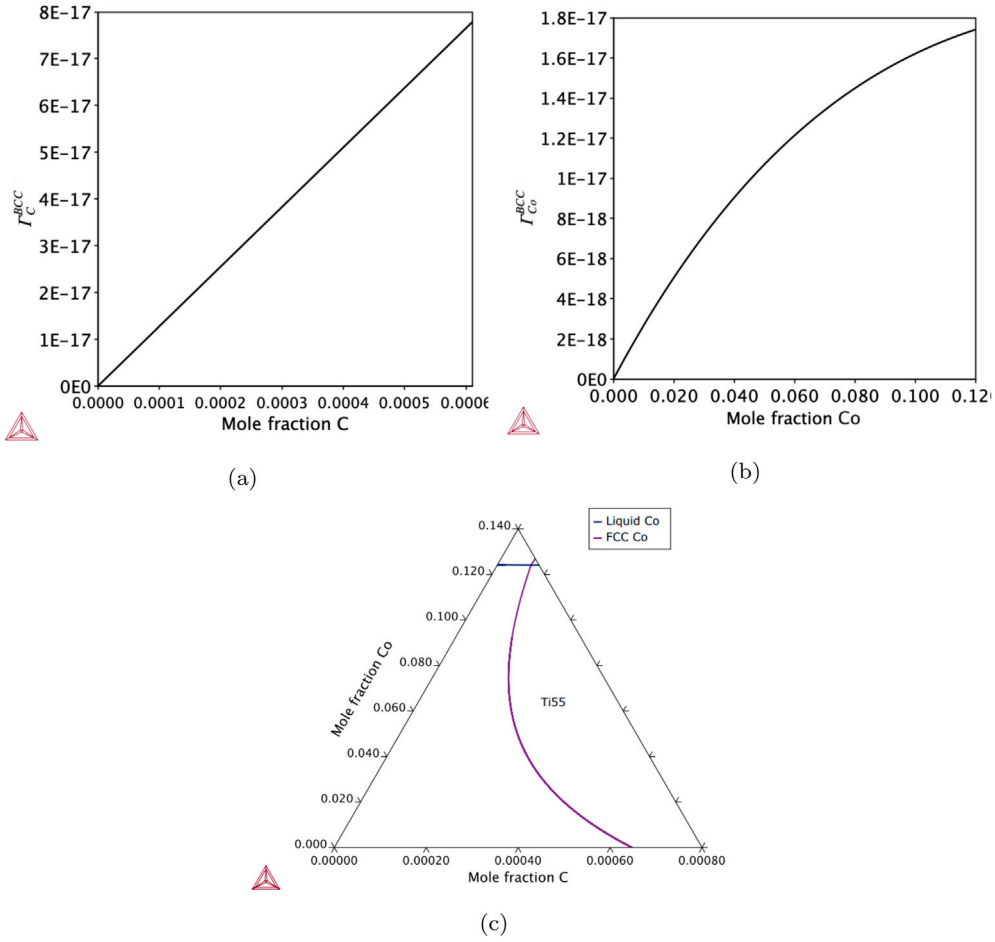

Fig. 9. Calculated permeabilities (mobility times solubility) and solubilities of C and Co in Ti–Al(5%)-V(5%) at 1000 °C. (a) permeability of C in Ti–Al(5%)-V(5%), (b) permeability of Co in Ti–Al(5%)-V(5%), (c) isopleth section showing solubility of C and Co in Ti–Al(5%)-V(5%).

Figs. 10 and 11 show the schematic illustration and thermodynamic calculations for two extreme cases considering only the tungsten carbide, respectively:

1. In the first extreme case (see Figs. 10(a), 11(a) and 11(b)), the activity of C is roughly fixed while the mass fraction of Co is varied. Fig. 11(a) shows that, by removing Co, the fraction of the binder phase decreases but there are no phase transitions. Fig. 11(b) shows the corresponding variation in C content when varying the cobalt content.
2. In the second extreme case (see Figs. 10(a), 11(c) and 11(d)), the carbon content is fixed, while again, the cobalt mass fraction is varied. Fig. 11(d) shows the corresponding C activity profile. While gradually removing Co from the system, the following observations can be made. While the activity of C is larger than 0.2, WC and the Co binder are the only stable phases. By removing more Co, the activity of C falls between 0.15 and 0.20, and η (M12C) becomes stable. When the Co content is less than 0.03 mass fraction, and the activity of C is between 0.05 and 0.1, η (M6C) becomes stable, and finally when the Co mass fraction is less than $2.5 \cdot 10^{-3}$ and the activity of C is less than 0.05, W(bcc) becomes stable. There are other stable phases with negligible phase fractions ($< 1 \cdot 10^{-3}$).

The thermodynamic calculations shown in Fig. 11 can be compared with the results obtained from the two diffusion simulations which are shown in Figs. 12 and 13. The simulation presented in Fig. 12 corresponds to the case of fixed C activity which can be considered to be closer to the case of turning than a diffusion couple. On the other

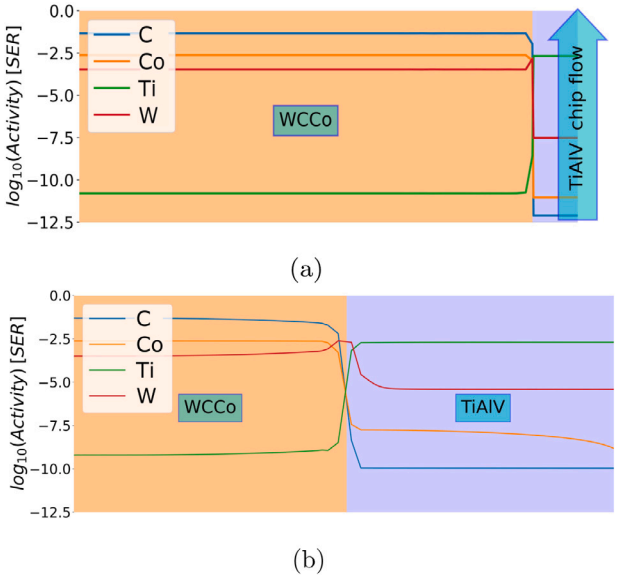

Fig. 10. Schematic illustration of obtained log_{10} activities of T, C, Co, W for: (a) roughly fixed C activity, and (b) the fixed carbon content simulation at 1000 °C. Solid lines represent 3600 s and dashed lines are the initial profile.

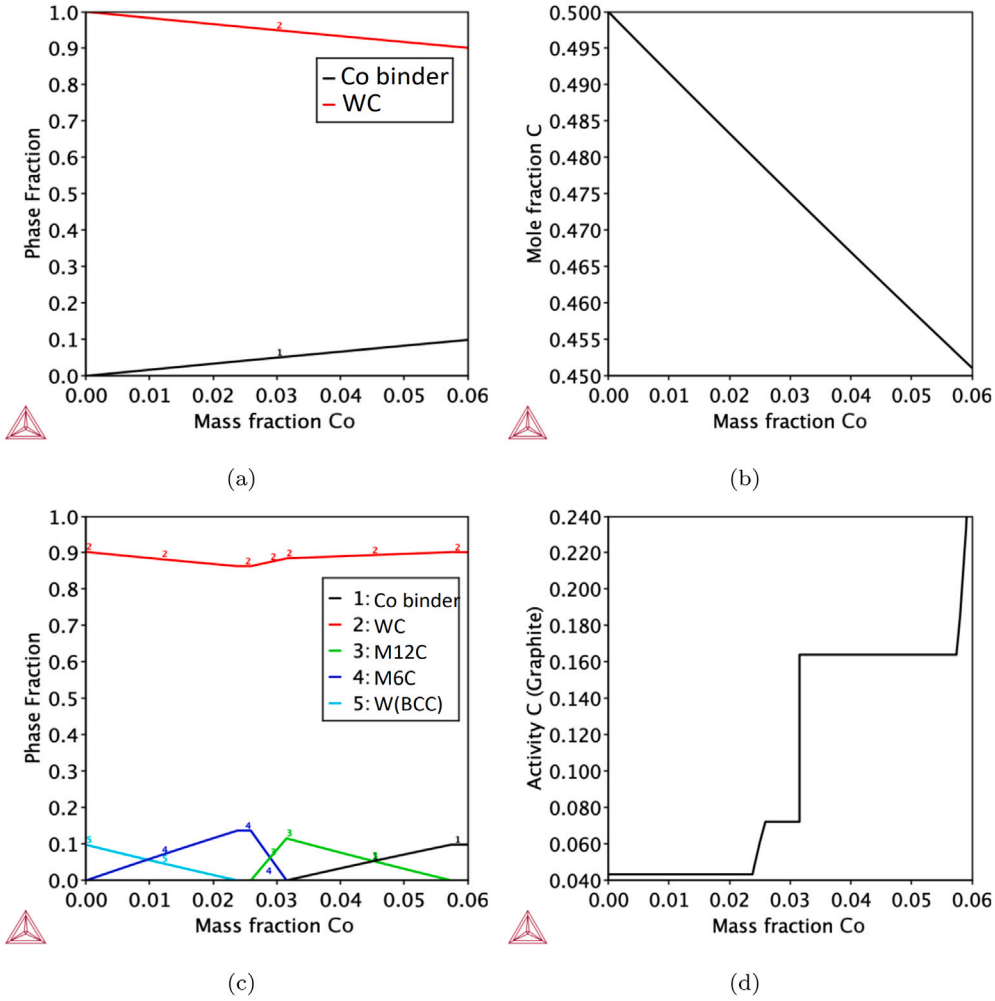

Fig. 11. Thermodynamic calculations of phase stability in the WC–Co(6%) system at 1000 °C while removing Co. (a) phase stability under roughly fixed C activity, (b) mole fraction of C under fixed C activity, (c) phase stability under fixed C content, (d) Activity of C under fixed C content.

hand, the simulation presented in Fig. 13, represents a case when the C activity is not fixed but the mass fraction of C is. The composition profiles in Figs. 12 and 13 have been plotted as so-called u-fractions. In this case, where there is only one interstitial element (C), the u-fraction is given by $u_L = \frac{x_L}{1-x_C}$ where x_L is the mole fraction of element L.

Figs. 12(a) and 12(b) shows how the system can be expected to behave when C activity is fixed; the obtained u-fraction profiles in these figures are obtained using the first extreme case (when C content is fixed). Due to the low permeability of Ti, Al and V in the Co binder, the formation of carbides is not possible. The sharp decrease in C activity (see Fig. 12(c)) results in precipitation of a small amount of η (M12C, M6C). However, the activity of C is never low enough for W(bcc) to precipitate.

In Figs. 13(a) and 13(b), the simulated u-fraction profiles of the WC–Co(6%),Ti–Al(5%)-V(5%) diffusion couple at the beginning and end of the simulation is illustrated. Fig. 13(a) shows the u-fraction profiles of substitutional elements, while Fig. 13(b) shows the u-fraction profile of C. A large integral change in the u-fraction of Co and a sharp peak in the u-fraction of carbon are observed at the interface. The sharp C peak corresponds to the formation of a TiC layer adjacent to Ti–Al(5%)-V(5%) (Fig. 13(d)). The zone showing a gradual decrease in Co u-fraction corresponds to the formation of η (M12C and M6C) and W(bcc). At higher Co u-fractions close to the WC–Co(6%), η (M12C) precipitation is observed while at lower Co u-fractions at the interface η (M12C), and W(bcc) forms. The order of precipitation depends on the C activity profile as it is shown in Figs. 11(c), 11(d) and 13(c).

5. Discussion

As established within the simulation results, the reaction diffusion and the resulting interface between the tungsten carbide and Ti alloy is governed by the unidirectional carbon and cobalt diffusion from the tungsten carbide and into the Ti alloy. The simple but highly illustrative thermodynamic calculations for the WC–Co(6%) and Ti–Al(5%)-V(5%) system was made for two extreme cases: (1) C activity was roughly fixed and the mass fraction of Co varied, (2) C content was fixed while Co was varied. These two conditions were chosen as it stands to reason that a diffusion couple, which is static in nature, would be analogous to (2) as C activity should decrease as equilibrium is approached, whereas, in a dynamic process, such as turning, where C is constantly being removed from the system, the C activity will remain higher for much longer, and therefore resemble a system between (1) and (2); see further discussion below. Indeed, if the tungsten carbide is also considered to be removed progressively, the system may never reach equilibrium and so a constant C activity is more relevant. In the extreme case where C content was fixed while Co was varied the diffusion of C will if unhindered, result in the formation of titanium carbide; the solubility limit of C in the Ti alloy is relatively low, roughly $6 \cdot 10^{-4}$ (mole fraction) [25]. Therefore, for the case of a diffusion couple, in which there is a non-equilibrated Ti alloy layer, the simulated result is shown in Fig. 13(d); the C profile has a sharp step at the interface, and a layer of TiC forms as soon as C content exceeds the solubility limit of C in Ti–Al(5%)-V(5%) ($\approx 6 \cdot 10^{-4}$ mole fraction at 1000 °C).

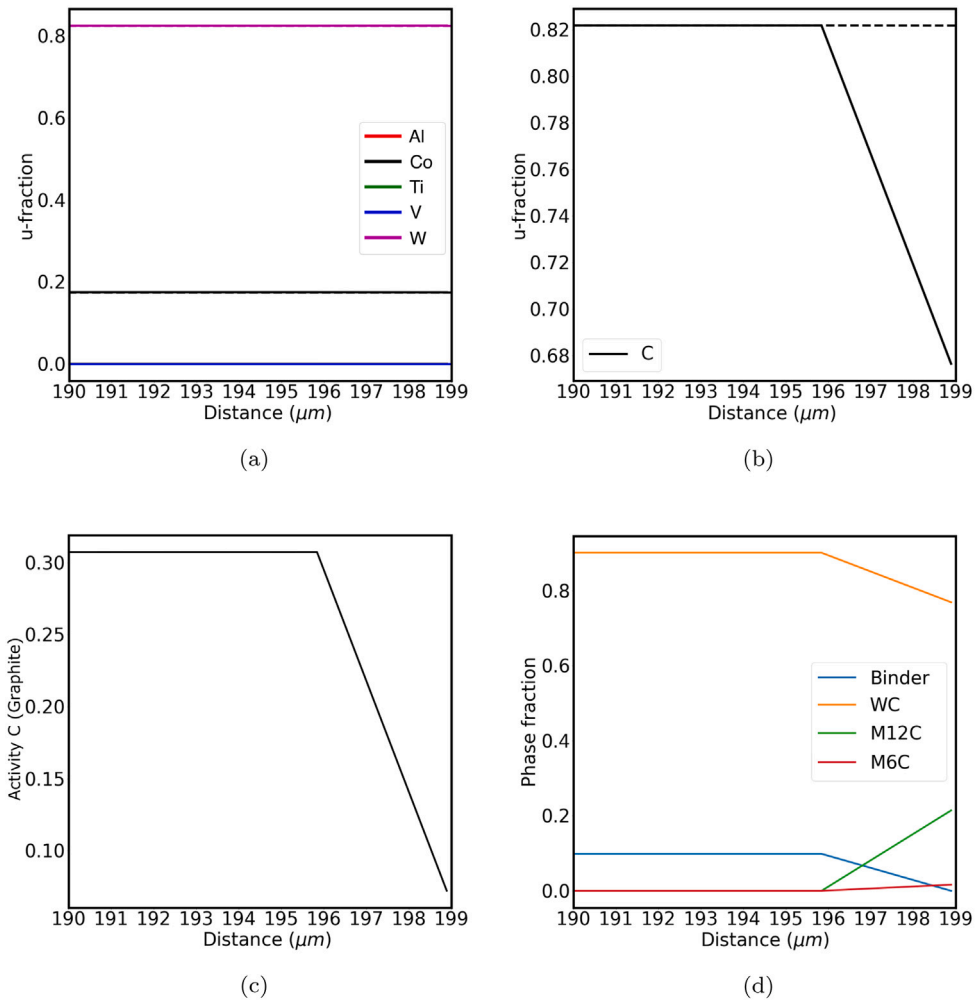

Fig. 12. Obtained u-fraction profiles, phase fractions, and C activity of the roughly fixed C activity simulation at 1000 °C. Solid lines represents 3600 s and dashed lines are the initial profile. (a) u-fractions of substitutional elements, (b) u-fraction of C, (c) C activity (d) phase fractions.

Subsequently, the TiC layer grows towards the Ti–Al(5%)-V(5%) and becomes thicker.

In the diffusion couple experiment, for which results are presented in Figs. 3 and 4, and in similar diffusion couples manufactured by other researchers [13,15,16], the TiC layer can be observed and is of a relatively similar size to that indicated by the simulation. The simulation also shows that the high solubility limit of Co in Ti–Al(5%)-V(5%) ($\approx$ 0.12 mole fraction at 1000 °C, (see Fig. 9)), results in a long diffusion distance of Co in Ti–Al(5%)-V(5%). This is because the diffusion of Co into the Ti alloy occurs at an anomalously fast rate [26]. The permeability (the product of solubility and diffusivity) of C and Co in Ti(bcc) is actually of the same order. Since the diffusion of Co in Ti(bcc) is very much faster than the diffusion of Ti in fcc-Co this process by itself could result in the formation of Kirkendall porosity, which could possibly be indicated by the darkest regions shown within the SEM image in Fig. 3. This is further supported by the fact that said dark regions are lacking in all elements within the system as shown by the WDS maps in Fig. 3. The relatively low pressure used during the manufacture of the diffusion couples could exacerbate possible Kirkendall porosity, while higher loads, such as those in machining processes, could be high enough to compress and eliminate such porosity. The formation of the TiC layer in combination with the depletion of cobalt from WC–Co(6%) causes a fixed carbon composition in the Co binder which triggers the formation of overlapping layers of reaction products. Depending on the distance from the WC–Co(6%) interface, different phases form in the following order: η (M12C), the next layer contains η (M6C) and W(bcc), and TiC forms at the Ti–Al(5%)-V(5%) interface. Evidence of all three of these phases is present within the WDS scan and SEM images given in Figs. 3 and 4, which are from the diffusion couple experiment.

The case of turning can be considered to be in between case 1 and 2 with close to roughly fixed C activity. This is because when the adhesive layer is removed due to turning conditions, or a steady state flux of carbon and cobalt through a thin adhesive layer transports C and Co to the Ti–Al(5%)-V(5%) chip flow, C content in the chip or adhesive layer will not exceed the solubility limit. According to the simulation, if the solubility limit is never reached, there would be no formation of TiC nor W(bcc). In reality, at the interface between tungsten carbide and the Ti alloy within the crater [17,18], there is no consistent TiC layer, yet there is evidence of TiC in isolated regions and evidence of W(bcc). These discrepancies can be explained by examining the current mechanistic understanding of the titanium WC–Co system in crater wear where there are two zones where C is lost from substrate [17,18]. In one zone, for which there is evidence of low C activity W(bcc) forms in a fringe-like morphology, this region exists for the majority of the interface. In the second zone, which is shown to exist at prior Co-rich regions, the formation of TiC has been evidenced.

Fig. 14 is a schematic diagram of the interface within the crater, highlighting the two zones at the interface. The simulation results presented in Fig. 11 indicate that when there is no Co, C activity will be low and only W(bcc) phase will form, like in the first zone where fringe like W(bcc) forms. An increase of C activity in the prior Co

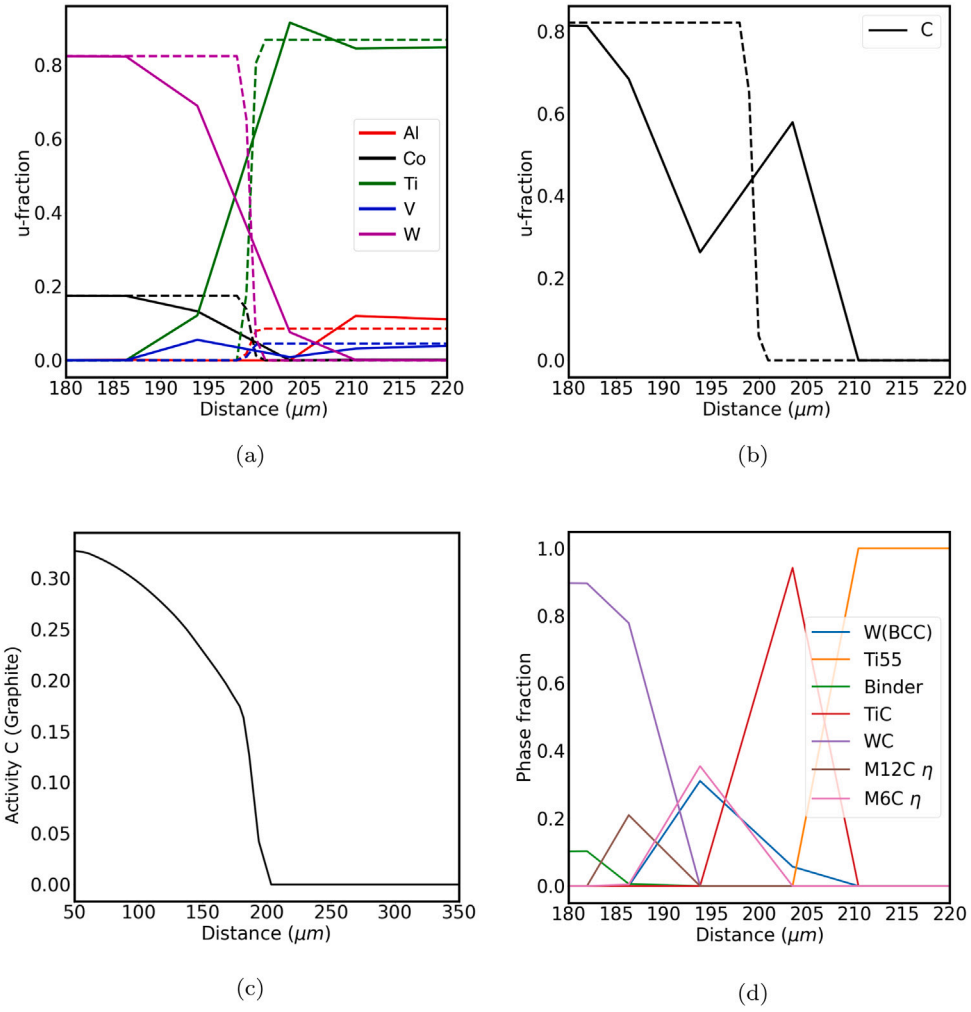

Fig. 13. Obtained u-fraction profiles, phase fractions, and C activity of the WC–Co(6%),Ti–Al(5%)-V(5%) diffusion couple at 1000 °C. Solid lines represents 3600 s and dashed lines are the initial profile. (a) u-fractions of substitutional elements, (b) u-fraction of C, (c) C activity, (d) phase fractions.

regions, where Co content exceeds 0.025 Co, is shown in the simulation and experiment. This theory leaves one unexplained phenomenon: interpreting the simulation in this way indicates there should be at least a small amount of η-phase (M6C or M12C) forming. It could be possible that it is as of yet undetected, especially since the sites of higher C activity are relatively rare and are difficult to analyse but further work would need to be carried out to investigate this. It is also important to consider that the simulations are conducted in 1D and so cannot account for 2D and even 3D interaction within the system which could restrict the formation of the η-phases.

In this work the utility of an accurate thermodynamic description is demonstrated by the following findings and discussion: Considering that in turning, which at the interface is analogous to the simulated case of roughly fixed C activity, it is probable that if C is continually removed from such regions, C will be depleted from ever-increasing distances below the subsurface, especially where the Co matrix acts as a diffusion pathway. This is because although the WC–Co system remains in equilibrium at 1000 °C [7], Co mono-layers between WC grains within the substrate [8], and constant C activity at the crater interface could disrupt the equilibrium, enables the removal of C from below the tool subsurface, and result in the formation of W(bcc). The so-called Co mono-layers will simultaneously act as a diffusion pathway for the C and, as the simulation in Fig. 11(c) suggests, promote the formation of W(bcc). Indeed, within Fig. 7 the comparison between the crater subsurface and centre of the tool shows the possible formation of W(bcc) at a WC–WC grain boundary for the former. Fig. 8 provides further evidence by way of EDP that it is W(bcc) forming 4 μm below the interface, and thus that C has been removed from the WC at such depths. The locations where W(bcc) is detected are often aligned with the chip flow direction, over the rake face of the tool. Although found during turning steel, thermomechanical loading in this manner is known to cause the formation of low energy planes near WC–WC boundaries within the substrate which could further disrupt the WC–Co equilibrium and explain why the W(bcc) is only located at WC–WC grain boundaries [10]. W(bcc) is weaker and more ductile than WC. Therefore, the formation of W(bcc) between WC grains below the subsurface of the crater could have catastrophic implications for the tool integrity, possibly contributing to the extreme loading of certain WC grains and promoting the high defect density which is highlighted in Fig. 5.

It has been reported many times that once the crater reaches a critical size the rate at which the tool wears via flank degradation and plastic deformation increases substantially [4]. This has always been considered to be due to the fact that the crater depth becomes so substantial that the nose of the tool can no longer withstand the mechanical load required during machining. However, the results of this work suggest it may also be in part due to substantial C removal from further into the tool which compromises its integrity. Such C removal would become faster and from greater distances under the subsurface as the crater size increases. Whilst investigating the subsurface decarburisation of the substrate, very clear evidence was found that, as mentioned previously, there exists a high defect density close below the

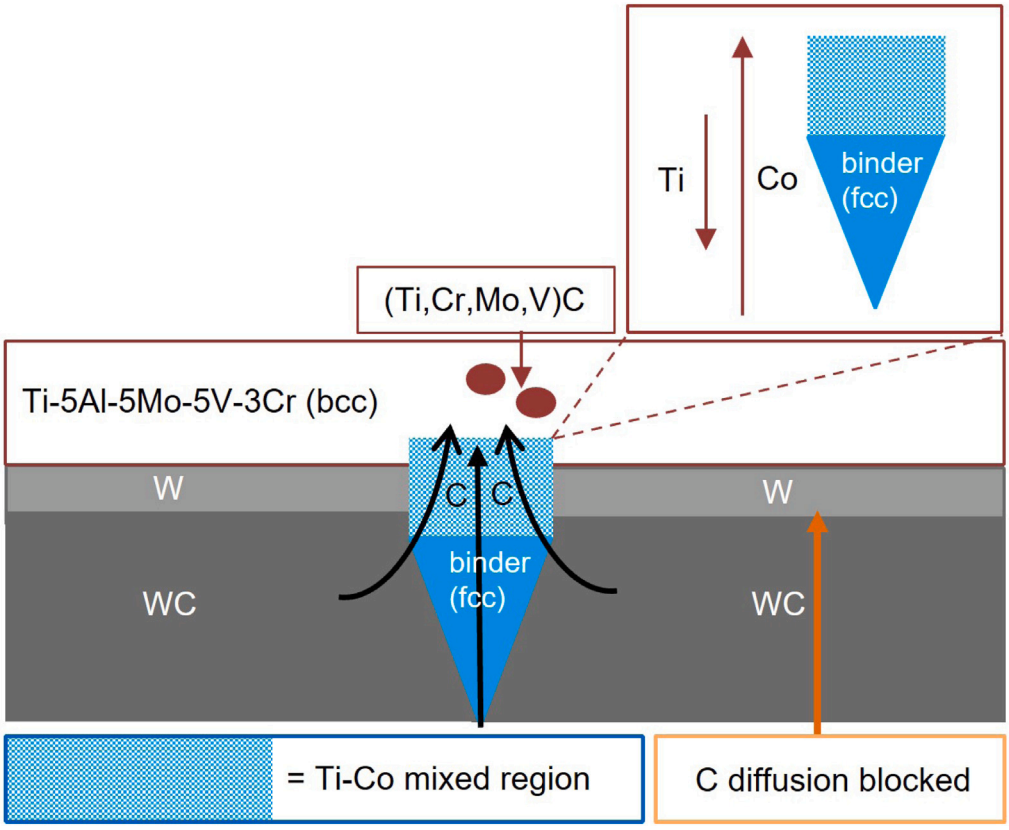

Fig. 14. Schematic diagram of the interface, within a crater, between WC–Co(6%) substrate and Ti–Al(5%)-V(5%)-Mo(5%)-Cr(3%).

crater interface; the TEM results in Fig. 5 showed that the number of defects was much higher near the subsurface of the crater than in the centre of the tool. This work marks the first time such damage has been imaged at such a resolution within the subsurface of WC–Co tools used to turn titanium. The extent of the defects demonstrates a substantial reduction in integrity and provides an insight into how the tool is damaged during the machining process. In Fig. 6d the fourier-filtered lattice shows the defects to be both stacking faults (encircled) and dislocations. The defect density within this region was calculated to be $\sim 5 \cdot 10^{15}/\mathrm{m}^2$. Such defect density demonstrates the mechanical loading that is induced at the crater subsurface and will play a significant role in the breakage of the tool.

6. Conclusions

This work examines the phenomenon of crater wear in titanium turning. This was achieved by linking the observable characteristics of an experimentally produced WC–Co Ti-5553 diffusion couple, with a similar interface from the rake face of a used turning insert, using thermodynamic calculations and kinetic simulations. The results can be summarised in the following points:

- The multilayered interface observed in diffusion couples containing titanium, TiC, η (M6C and M12C) and WC–Co substrate occurs due to a fixed C content. For the case of a static system (diffusion couple), as C and Co are removed from the substrate, there exist critical levels of C and Co activity that result in the formation of each of the aforementioned layers.
- Each zone seen within the crater interface formed after turning have been experimentally confirmed to occur at either regions with low Co, where W(bcc) forms, or high Co where TiC forms.
- The simulations suggest that for the case of turning, C and Co will be lost continuously resulting in their removal from the substrate. The loss of carbon and corresponding dissolution of W within the substrate and subsequent formation of W(bcc) at 4 μm below the crater interface at WC–WC grain boundaries was proven using TEM.
- When examining the subsurface of the tool, the WC grains at 2 - 4 μm, were shown, for the first time, to have a high defect density compared to those within the bulk of the tool. This will reduce the integrity of the tool, increasing the propensity for critical failure.

The thermodynamic description of the WC–Co system explains for the first time the unresolved discrepancies between the static diffusion couple and dynamic crater interface of the titanium WC–Co system. This provides a key step to base future work upon. Already, the utility of having an accurate description of the system has been demonstrated, by improving the current understanding of the mechanism by which the integrity of the tool material is reduced: subsurface decarburisation.

Declaration of competing interest

The authors declare that they have no known competing financial interests or personal relationships that could have appeared to influence the work reported in this paper.

Data availability

No data was used for the research described in the article.

Acknowledgements

We thank Dr Pete Crawforth and the Advanced Manufacturing Research Center for their assistance in this work. We acknowledge Sandvik Coromant for their support. The authors would also like to thank the Henry Royce Institute for Advanced Materials, EPSRC, United Kingdom grants EP/L016257/1. This work was partly funded by the Swedish Foundation for Strategic Research (SSF), contract RMA15-0062.

References

[1] J.D. Cotton, R.D. Briggs, R.R. Boyer, S. Tamirisakandala, P. Russo, N. Shchetnikov, J.C. Fanning, State of the art in beta Titanium alloys for airframe applications, Jom (ISSN: 15431851) 67 (6) (2015) 1281–1303.

[2] E. Ezugwu, Z. Wang, Titanium alloys and their machinability, J. Mater Process. Technol. (ISSN: 09240136) 68 (3) (1997) 262–274, arXiv:arXiv:1011.1669v3. http://www.sciencedirect.com/science/article/pii/S0924013696000301.

[3] P.J. Arrazola, A. Garay, L.M. Iriarte, M. Armendia, S. Marya, F. Le Maître, Machinability of titanium alloys (Ti6Al4V and Ti555.3), J. Mater Process. Technol. (ISSN: 09240136) 209 (5) (2009) 2223–2230.

[4] P.D. Hartung, B. Kramer, B. Von Turkovich, Tool wear in titanium machining, CIRP Ann. 31 (1) (1982) 75–80.

[5] P.A. Dearnley, A.N. Grearson, Evaluation of principal wear mechanisms of cemented carbides and ceramics used for machining titanium alloy IMI 318, Mater. Sci. Technol. (United Kingdom) (ISSN: 17432847) 2 (1) (1986) 47–58.

[6] S. Odelros, Tool wear in titanium machining, 31 (2012) 75–80.

[7] M. Walbrühl, D. Linder, J. Ågren, A. Borgenstam, Diffusion modeling in cemented carbides: solubility assessment for Co, Fe and Ni binder systems, Int. J. Refract. Met. Hard Mater. 68 (2017) 41–48.

[8] A. Henjered, M. Hellsing, H. Andrén, H. Nordén, Quantitative microanalysis of carbide / carbide interfaces in WC – Co-base cemented carbides microanalysis of carbide / carbide interfaces in cemented carbides, 0836 (1986).

[9] G.S. Upadhyaya, Cemented tungsten carbides, properties and testing, 1998.

[10] G. Östberg, K. Buss, M. Christensen, S. Norgren, H.O. Andrén, D. Mari, G. Wahnström, I. Reineck, Mechanisms of plastic deformation of WC-Co and Ti(C, N)-WC-Co, Int. J. Refract. Met. Hard Mater. (ISSN: 02634368) 24 (1–2) (2006) 135–144.

[11] A. Jawaid, C.H. Che-Haron, A. Abdullah, Tool wear characteristics in turning of titanium alloy Ti-6246, J. Mater Process. Technol. (ISSN: 09240136) 92–93 (1999) 329–334.

[12] S. Saketi, S. Odelros, J. Östby, M. Olsson, Experimental study of wear mechanisms of cemented carbide in the turning of Ti6Al4V, Materials (ISSN: 19961944) 12 (7) (2019).

[13] B. Kaplan, S. Odelros, M. Kritikos, R. Bejjani, S. Norgren, Study of tool wear and chemical interaction during machining of Ti6Al4V, Int. J. Refract. Met. Hard Mater. (ISSN: 22133917) 72 (2018) 253–256, http://dx.doi.org/10.1016/j.ijrmhm.2017.12.012.

[14] L. Fieandt, R. M'Saoubi, M. Schwind, B. Kaplan, C. Århammar, B. Jansson, Chemical interactions between cemented carbide and difficult-to-machine materials by diffusion couple method and simulations, J. Phase Equilib. Diffus. (ISSN: 15477037) 39 (4) (2018) 369–376.

[15] O. Hatt, Z. Lomas, M. Thomas, M. Jackson, The effect of titanium alloy chemistry on machining induced tool crater wear characteristics, Wear (ISSN: 00431648) 408–409 (2018) 200–207, http://dx.doi.org/10.1016/j.wear.2018.05.020.

[16] C. Ramirez, A. Idhil Ismail, C. Gendarme, M. Dehmas, E. Aeby-Gautier, G. Poulachon, F. Rossi, Understanding the diffusion wear mechanisms of WC-10%Co carbide tools during dry machining of titanium alloys, Wear (ISSN: 00431648) 390–391 (July) (2017) 61–70, http://dx.doi.org/10.1016/j.wear.2017.07.003.

[17] A. Graves, S. Norgren, W. Wan, S. Singh, M. Kritikos, C. Xiao, P. Crawforth, M. Jackson, On the mechanism of crater wear in a high strength metastable beta titanium alloy, Wear (ISSN: 00431648) 484–485 (March) (2021) 203998, http://dx.doi.org/10.1016/j.wear.2021.203998.

[18] R. Lindvall, F. Lenrick, R. M'Saoubi, J.-E. Ståhl, V. Bushlya, Performance and wear mechanisms of uncoated cemented carbide cutting tools in Ti6Al4V machining, Wear (ISSN: 0043-1648) 477 (2021) 203824, 23rd International Conference on Wear of Materials. https://www.sciencedirect.com/science/article/pii/S0043164821002131.

[19] M. Lattemann, E. Coronel, J. Garcia, I. Sadik, Interaction between cemented carbide and Ti6Al4V alloy in cryogenic machining, in: 19. Plansee Seminar 2017, 2017, pp. 1–13.

[20] H. Larsson, L. Höglund, Multiphase diffusion simulations in 1D using the DICTRA homogenization model, (ISSN: 0364-5916) 33 (3) (2017) 495–501, (Sept. 2009). https://www.sciencedirect.com/science/article/pii/S0364591609000522.

[21] H. Larsson, A model for 1D multiphase moving phase boundary simulations under local equilibrium conditions, (ISSN: 0364-5916) 47 (2018) 1–8, (2014). http://www.sciencedirect.com/science/article/pii/S0364591614000492.

[22] J.-O. Andersson, T. Helander, L. Höglund, P. Shi, B. Sundman, Thermo-Calc & DICTRA, computational tools for materials science, Calphad 26 (2) (2002) 273–312.

[23] Thermo-Calc software TCFE steels/Fe-alloys thermodynamic database version 9, 2020, accessed 8-2-2020.

[24] Thermo-calc software MOBFE steels/Fe-alloys mobility database version 5, 2020, date accessed 8-2-2020.

[25] K. Frisk, A revised thermodynamic description of the Ti–C system, CALPHAD 27 (4) (2003) 367–373.

[26] H. Nakajima, M. Koiwa, Diffusion in titanium, ISIJ Int. 31 (8) (1991) 757–766.